

An object-based conceptual framework and computational method for representing and analyzing coastal morphological changes

Hongxing Liu^{a*}, Lei Wang^b, Douglas Sherman^c, Yige Gao^c and Qiusheng Wu^a

^a*Department of Geography, University of Cincinnati, Cincinnati, OH, USA;* ^b*Department of Geography and Anthropology, Louisiana State University, Baton Rouge, LA, USA;* ^c*Department of Geography, Texas A&M University, College Station, TX, USA*

(Received 21 July 2009; final version received 4 August 2009)

This article presents an object-based conceptual framework and numerical algorithms for representing and analyzing coastal morphological and volumetric changes based on repeat airborne light detection and ranging (LiDAR) surveys. This method identifies and delineates individual zones of erosion and deposition as discrete objects. The explicit object representation of erosion and deposition zones is consistent with the perception and cognition of human analysts and geomorphologists. The extracted objects provide ontological and epistemological foundation to localize, represent, and interpret erosion and deposition patches for better coastal resource management and erosion control. The discrete objects are much better information carriers than the grid cells in the field-based representation of source data. A set of spatial and volumetric attributes are derived to characterize and quantify location, area, shape, orientation, depth, volume, and other properties of erosion and deposition objects. Compared with the conventional cell-by-cell differencing approaches, our object-based method gives a concise and high-level representation of information and knowledge about coastal morphological dynamics. The derived attributes enable the discrimination of true morphological changes from artifacts caused by data noise and processing errors. Furthermore, the concise object representation of erosion and deposition zones facilitates overlay analysis in conjunction with other GIS data layers for understanding the causes and impacts of morphological and volumetric changes. We have implemented a software tool for our object-based morphological analysis, which will be freely available for the public. An example is used to demonstrate the utility and effectiveness of this new method.

Keywords: coastal changes; morphology; object-based shape and volumetric attributes; LiDAR

1. Introduction

The coastal zone is one of the most dynamic yet vulnerable geomorphic environments on earth. Various processes shape and modify coastal morphology over a wide range of temporal and spatial scales. Information about spatial patterns of erosion and deposition and corresponding volumetric changes of the coastal zone is particularly important for assessing and predicting the impacts of tropical storms and hurricanes and for formulating intelligent management policies to mitigate and prevent potential damages to shorefront properties and infrastructure. Until recently, most morphological change studies for coastal areas have been based on ground surveys of transects perpendicular to the shoreline across

*Corresponding author. Email: Hongxing.Liu@uc.edu

the beach (Dolan *et al.* 1991), using the rod and level instruments or kinematic GPS system. In most cases, these transects are widely spaced and cover only a limited length of coastal reach at selected sites due to time and cost restrictions. Sparse sampling of beach profiles along transects provides only a coarse representation of the surface morphology of the beaches and sand dunes, which is often inadequate for an accurate and reliable estimate of volumetric changes of coastal morphology. Other studies, using total stations, have been able to provide morphological information at denser spatial sectors, but they are still limited in their total spatial coverage (e.g. Andrews *et al.* 2002).

The recent advent of airborne light detection and ranging (LiDAR) system represents a technological breakthrough in surveying, mapping, and monitoring coastal environmental conditions and changes. Airborne LiDAR data have been increasingly available for the coastal research community. Topographical LiDAR data along the US coastline have been collected through a partnership program jointly funded by NOAA, USGS, and NASA. A considerable length of the US coast has been surveyed repetitively by airborne LiDAR, and many LiDAR surveys were scheduled before and after major storm events. The LiDAR system offers an extraordinary capability in gathering highly accurate and densely sampled topography measurements in a quick, cost-effective manner. This allows for an entirely new level of detailed analysis of micro-geomorphology of the beach and sand dunes (White and Wang 2003, Finkl *et al.* 2005, Zhang *et al.* 2005). Repeat LiDAR surveys enable three-dimensional volumetric change analysis and thorough sediment budget estimation over a broad region (White and Wang 2003). With technological advancements come not only new opportunities but also challenges. The primary challenge facing the coastal research community is to develop new conceptual framework and efficient computational methods that can fully exploit high-resolution LiDAR data for information and knowledge extraction and representation (Brock *et al.* 2004).

In previous studies, the cell-by-cell differencing method was commonly adopted for the volumetric analysis based on sequential LiDAR surveys (Gutierrez *et al.* 2001, Sallenger *et al.* 2003, White and Wang 2003, Shrestha *et al.* 2005, Zhang *et al.* 2005, Gares *et al.* 2006). This method is conceptually based on the field-based data model, which views and represents the morphological and volumetric changes as a continuous field of elevation variation over the geographic space. The volume change is evaluated on a cell-by-cell basis by subtracting a post-event LiDAR digital elevation model (DEM) from a pre-event DEM. Similar to the cut-and-fill analysis used in civil engineering applications, a negative elevation difference indicates a cell where surface material was eroded (cut) between two LiDAR surveys. A positive value indicates the cell where sediment accretion (fill) occurred, and a zero value indicates a cell where there was no net change. Owing to the nature of the field-based representation, the cell-by-cell differencing method suffers from several drawbacks. Although the elevation difference grid can be visually interpreted by human analysts for a qualitative assessment of the spatial distribution of changes, individual erosion and deposition patches and zones are not explicitly represented. The cell-by-cell differencing method represents a low level of data processing, and the large volume of resulting difference values do not carry much explicit high-level information. Most previous studies only calculated and reported overall erosion, deposition, and net volume change for the entire study area, but the properties of distinct erosion and deposition regions were often ignored. In addition, volumetric calculations through cell-by-cell differencing are subject to data noise. It is difficult to recognize and correct artifact changes induced by data noise and data-processing errors on a cell-by-cell basis. A new conceptual framework and corresponding computational methods are needed to reap the potential of airborne LiDAR data for the understanding of coastal morphological changes.

This article presents an object-based conceptual framework for volumetric analysis of coastal morphological dynamics with repeat LiDAR data. The object-based data model views geographic reality as a surface occupied by a series of discrete and identifiable objects, which can be represented by geometric shapes and can be described by their properties (attributes). With the object-based conceptual framework, we develop algorithms to explicitly identify and delineate individual erosion and deposition zones (patches) as discrete objects, which are represented by a set of polygon features. These erosion and deposition objects, rather than individual grid cells, are subsequently used as basic spatial units for morphological analysis of coastal changes. Two-dimensional planimetric and three-dimensional volumetric properties are derived for these objects and included in the feature attribute table of the object polygons. The numerical algorithms have been implemented using the C++ programming language to perform object recognition and attribute derivation. The explicit object representation of erosion and deposition patches makes it easy to localize and represent the spatial distribution of erosion or deposition patches and to analyze the spatial pattern of morphological changes. The concise and localized information about sediment erosion and deposition is useful for coast managers to formulate intelligent decisions and policies for erosion control and coastal resource protection. The representation of erosion and deposition patches and zones as polygonal objects also facilitates overlay analysis in conjunction with other GIS data layers for exploring the causes and impacts of the volumetric and sediment changes. Furthermore, the derived morphological and shape attributes enable the discrimination of true morphological changes from spurious artifacts caused by data noise and data-processing errors. In the following sections, we present basic concepts, algorithms, and a software tool for the object-based morphological analysis. An example is used to demonstrate the computational procedure and the effectiveness of this new approach.

2. Morphological change analysis based on sequential LiDAR surveys

The airborne LiDAR system emerges as a result of the integration of three technological components: the laser scanner, differential GPS, and inertial measurement unit (IMU). The LiDAR system records the time difference between transmission of the laser beam and the reception of a reflected signal as well as the backscatter intensity of the return. By using the aircraft position and orientation information acquired by GPS and IMU, the laser range measurements can be converted to highly accurate spot elevation values (Sallenger *et al.* 2003). The Airborne LiDAR Assessment of Coastal Erosion project jointly funded by NOAA, NASA, and USGS has collected baseline coastal topographical data for the conterminous United States since 1996. The LiDAR data are archived at NOAA's Coastal Service Center and are available online to the public (<http://maps.csc.noaa.gov/TCM/>).

Morphological and volumetric analysis determines the quantity of sediment material that has been lost or gained in an area by comparing two surface models of the area: one before a change (event) and the other after the change (event). Two or more repeat LiDAR surveys of the same reach are required for volumetric change calculation. A number of pre-processing steps are necessary prior to the volumetric computation. First, the LiDAR data sets need to be referenced to a common datum and map projection. The vertical datum NAVD88 is widely used in the United States, which is an orthometric datum. The original WGS84 ellipsoidal heights from the LiDAR surveys can be converted to the elevation values referenced to the NAVD88 by using the latest geoid model GEOID03 developed by the National Geodetic Survey (NGS) (Parker 2003). The reliability and accuracy of volumetric change analysis depends on the relative accuracy between the sequential LiDAR surveys used. Possible systematic bias between repeat LiDAR surveys can be detected and removed through

vertical calibration based on pseudo-invariant features (PIFs). PIFs are stable natural or cultural features whose planimetric position (x, y coordinates) and elevation (z value) do not change between sequential LiDAR surveys. Random errors of LiDAR data can be reduced by applying a median or a Gaussian filter (Liu *et al.* 2007).

3. Conceptual framework for object-based analysis of morphological changes

A brief review of spatial conceptualization and representation schemes in Geographical Information Science (GIScience) is necessary to establish the theoretical context and notations for defining, delineating, and interpreting coastal morphological change objects (features). The continuous fields and discrete objects are the most widely accepted views and approaches to conceptualizing and representing geographical phenomena in the GIScience. The concept of object orientation was first introduced into the GIScience in the late 1980s (Egenhofer and Frank 1987). Since then, the object-oriented data model has been further explored and adopted in many studies (Egenhofer and Frank 1992, Usery 1993, Worboys 1994, Raper and Livingstone 1995, Tang *et al.* 1996, Usery 1996, Leung *et al.* 1999, Bian 2000, Arctur and Zeiler 2004). It should be noted that the object-based approach has also been adopted in other geoscience disciplines, prominently in landscape ecology (Turner and Gardner 1991, Forman 1995, Turner *et al.* 2001). With the object-based view, the landscape is treated as a mosaic of a variety of different ecologic patches (objects). A software tool 'FRAGSTATS' (McGarigal and Marks 1995, McGarigal *et al.* 2002) has been developed to compute a suite of metrics (attributes) for every patch and patch type in the landscape. The object-based approach has been recently introduced for analyzing remotely sensed imagery (Blaschke and Strobl 2001, Castilla and Hay 2008), and a commercial software tool 'eCognition/Definiens' has been dedicated to extract and quantify image objects (Baatz *et al.* 2001).

The field-object dichotomy has been actively discussed in the GIScience literature (Peuquet 1988, Couclelis 1992, Goodchild 1992, Peuquet 1994, Cova and Goodchild 2002, Galton 2004, Bian 2007). The consensus is that field-based and object-based representation models are compatible and complementary, rather than mutually exclusive and conflicting (Couclelis 1992, Galton 2001, Cova and Goodchild 2002, Goodchild *et al.* 2007). The transformations and interconvertibility between the field-based and object-based representations have been addressed in the GIScience literature (e.g. Camara *et al.* 1995, Gahegan 1996, Galton 2001). Although a geographical phenomenon can be conceptualized as either continuous fields or discrete objects, some forms of geographical phenomena are most naturally represented in terms of fields, and others lend themselves to expression in terms of objects. The selection of information to be represented and the choice of representational scheme have a profound impact on the efficiency and ease of use of a certain set of analytical operations and spatial models. It is also generally recognized that the way humans perceive, think, and communicate is more consistent with the object-based view (Couclelis 1992, Peuquet 1994, Smith and Mark 2003, Goodchild *et al.* 2007). Field-based representation is a 'rawer' form of data model, while object-based representation is a higher-level data model, capturing more semantics (meanings) of geographical features.

Previous coastal change studies are primarily based on the field-based representation. The cell-by-cell differencing operation was commonly applied to successive elevation measurements to extract coastal change information. The resulting elevation difference grid is the result of a low level of data processing for information extraction. Although the information about erosion and deposition is present in the large number of cells of elevation difference grid, it is in an implicit and 'rawer' form. Conventionally, human analysts and geomorphologists visually interpreted the elevation difference grid and perceptually organized the elevation

cells into various erosion and deposition patches (objects) to gain a higher level of information and knowledge about morphological and volumetric change patterns. At present, there is a strong need for a rich and flexible conceptual framework and numerical algorithms for extracting meaningful coastal morphological change objects (features) and deriving multifaceted attributes for the objects, which are ontologically and epistemologically fundamental to characterization and interpretation of coastal morphological changes.

We have developed a conceptual framework for the definition and ontology of coastal morphological change objects. To mimic human perception, erosion and deposition patches and zones are conceptualized and treated as a series of discrete, countable objects. Numerical algorithms have been developed and implemented for automated extraction of morphological change objects with the higher-level semantic information from low-level elevation difference grid. According to Smith and Mark (2003), the morphological change objects created from our numerical analysis belong to fiat objects, which exist only in virtue of demarcation of human cognition process and their boundaries may not correspond to observable discontinuity on the ground. Fiat objects are in contrast to bona fide objects, which exist independently of human cognition with determinate and prominent boundaries (Smith and Mark 2003). Given the basic dimensions of geographic phenomena such as space (location), theme, and time, we have implemented algorithms to derive sets of spatial, thematic, and temporal attributes for ontologically characterizing the states and conditions of the objects.

4. Creation of meaningful erosion and deposition objects

Before a geographic object can be counted, measured, and described, it must first be identified and delineated. Our computational method replicates the visual interpretation method used by geomorphologists, numerically extracting morphological change objects from the lower form of source data, namely, the field-based elevation difference grid.

Assume that two surface DEMs have been created from sequential LiDAR surveys at times t_1 and t_2 . Also assume that two DEMs are in a raster (grid) format with the same spatial resolution and they are referenced to a common map projection and datum (Figure 1a and b). The two LiDAR DEMs can be differenced for change analysis as in Equation (1):

$$\Delta z_{ij} = z_{ij}^{t_2} - z_{ij}^{t_1} \quad (1)$$

where $z_{ij}^{t_1}$ and $z_{ij}^{t_2}$ are the elevation values for the cell (i, j) , respectively, at time t_1 and time t_2 , and Δz_{ij} is the elevation difference for the cell (i, j) (Figure 1c). Negative difference values consist of the regions where the surface materials have been eroded, and positive differences indicate accretion. We consider a cell unchanged if its measured elevation difference is within the range of measurement error. The grid cells are coded into three categories (c_{ij}): erosion (−1), deposition (1), and unchanged (0).

$$c_{ij} = \begin{cases} 1, & \text{if } z_{ij} > k\sigma_d \\ -1, & \text{if } z_{ij} < -k\sigma_d \\ 0, & \text{if } -k\sigma_d \leq z_{ij} \leq k\sigma_d \end{cases} \quad (2)$$

where σ_d is the random error for difference measurements, k is multiplicative factor, commonly ranging from 1.0 to 3.0, and c_{ij} is the morphological change code for the grid cell (i, j) . Figure 1d shows the morphological change codes for the hypothetical example with $k = 2.0$ and $\sigma_d = 0.2$ m.

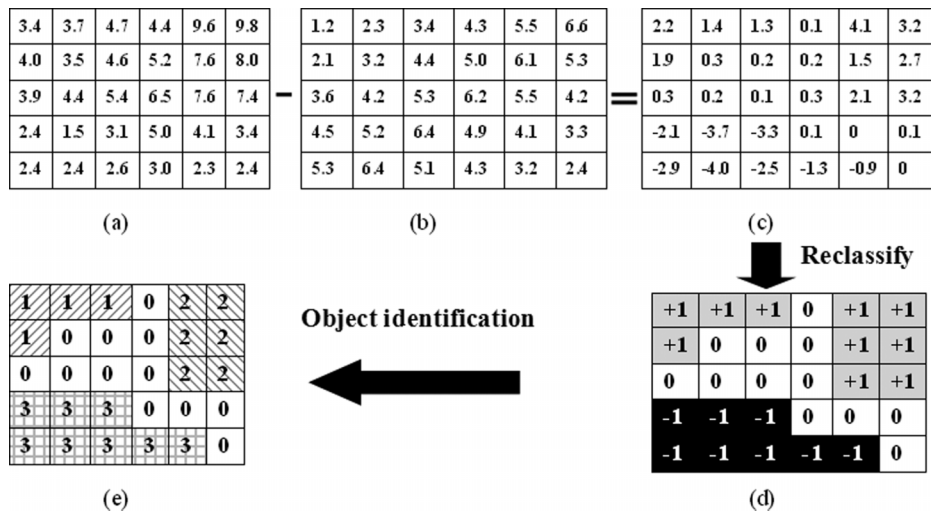


Figure 1. Identification of erosion and deposition objects. (a) DEM at time T_2 ; (b) DEM at time T_1 ; (c) elevation difference values; (d) morphological change classification with $k = 2$ and $\sigma_d = 0.2$ m; and (e) resulting erosion and deposition objects with ID numbers.

In the object-based morphological change analysis, we focus on erosion and deposition patches and zones, which are modeled as individual objects. The unchanged cells are treated as the background and ignored in the subsequent analysis. As such, the identified objects are mutually disjointed and do not exhaustively cover the space of the original field-based elevation grid. To measure their spatial and volumetric properties, erosion and deposition patches and zones need to be explicitly marked out and numerically represented as discrete objects. Numerically, a discrete erosion object is defined as a continuous spatial aggregation of connected erosion cells. Two erosion cells are considered to be spatially connected if they are connected by a path that consists of a series of adjacent erosion cells. Two cells are said to be adjacent to each other if one is located in the immediate four neighborhoods (horizontal and vertical neighbors) of the other, excluding the four diagonal neighbors. A recursive, connected-component labeling algorithm (Sonka *et al.* 1999, Liu and Jezek 2004) is used to computationally identify and index erosion objects based on the spatial connectivity of erosion cells. First, the elevation difference grid is scanned in a row-wise manner, and a seed is set at the first erosion cell. This single-cell erosion object is expanded to include all erosion cells located in its immediate neighborhood. The expansion is continued recursively until all connected erosion cells are included. The first erosion object is thus delineated and labeled. Then, the recursive expansion process is repeated to identify next erosion object. The erosion objects are indexed incrementally with a unique integer. Using the same computational procedure, deposition objects can be formed and indexed as well. The objects of the same type (erosion or deposition) are spatially detached from each other. However, a deposition object may be adjacent to one or more erosion objects, and vice versa. The two passes of object identification (ID) operations create disjointed erosion objects and deposition objects embedded in the background of unchanged cells. Figure 1e shows the resulting erosion and deposition objects with ID numbers.

When high-resolution LiDAR data are used, the delineated objects may be subject to errors for various reasons, including data noise, residual horizontal alignment error, interpolation error, resolution limitation, or the presence of movable objects like vehicles, people, and large

animals. Some small erosion and deposition objects may be fictitious, and some objects may contain small holes and breaks. The object boundaries may have spurious microlevel indentations and overhangs. To correct these errors, three types of morphology operations are applied. First, a closing operation (Sonka *et al.* 1999) is applied to the objects. The closing operation consists of a dilation operation immediately followed by an erosion operation. The dilation operation adds cells to the perimeter of each object and thus potentially closes broken areas. The erosion operation etches cells away from the perimeter of each object and therefore shrinks the object. The closing operation effectively smoothes rough boundaries and closes small gaps in objects. Then, a fill operation is applied to close small interior holes and cavities with a size smaller than the specified threshold. Finally, a trim operation is applied to eliminate those isolated objects that are smaller than the other specified threshold.

After removing spurious objects and smoothing object boundaries through morphological operations, a set of clean and reliable erosion and deposition objects are obtained. A boundary tracing and vectorization algorithm (Liu and Jezek 2004) is then applied to mark the boundary of each object and represent it as a polygon feature. At this stage, the basic spatial units for the morphological analysis have been changed from grid cells to morphological objects. With the change in the surface representation from the continuous field view to the object view, the information and semantics are enriched in the form of identified, structured objects and associated attributes. After vectorization, a polygon attribute table (PAT) is associated with the vector polygon feature of the erosion and deposition objects in the ArcGIS shape file format. The table contains object ID numbers and various spatial and volumetric properties of corresponding objects (as described in the next section). The vector polygon data can be displayed, edited, and analyzed in a GIS environment in association with other data layers.

5. Attribute derivation for characterizing erosion and deposition objects

A geographical object can be represented by three basic elements: identifier, state, and behavior. During the object extraction stage, a unique ID number is assigned to each object providing a way to distinguish an object from others. The state of an object is characterized by a set of attributes (semantic properties) at a given time. The dynamic behavior of an object describes processes acted on the object. Processes lead to changes in the state of an object, and the object's dynamic behavior can be represented as changes in attribute values. We encapsulate each object as an integrated, self-contained package of the identifier and as a multitude of static and dynamic attributes. The object identifier provides an interface to access the attributes.

We have computed five categories of attributes from sequential LiDAR data to describe and quantify spatial, thematic, and temporal dimensions of morphological objects. Those include planimetric attributes, shape attributes, surface attributes, volumetric attributes, and summary statistical indicators. Other thematic attributes may be computed for the discrete objects if ancillary data layers like multispectral remote-sensing images are incorporated in the analysis. When measuring fundamental geometric and shape properties, the objects are treated as homogeneous entities. In the process of object extraction, we disregard within-object variance and subtlety in the original data from which objects were formed. The increased utility offered by additional object attributes overwhelms the loss of precision in the formation of objects. Subtle within-object variations cannot be completely kept in the object-based representation, but the internal composition and heterogeneity for each object can be statistically summarized in a coarse fashion using selected statistical variables. For instance, the mean (or median) of vertical elevation changes can be computed for

characterizing the central tendency of elevation changes inside an object. The range (minimum and maximum values) and standard deviation of elevation changes can be calculated for indicating internal heterogeneity of elevation changes within the object. The aggregate and distribution properties of the objects can be measured in terms of different types of objects, different subdivision of regions, or across the entire scene (landscape) under consideration.

It should be noted that this research aims to provide a general analytical framework and software tool for object-based morphological analysis. For this reason, we intentionally include some similar alternative attributes in each category because specific applications and users may prefer different forms of attributes for representing particular aspects of morphology. Therefore, some derived attributes may be partially or completely correlated. For a specific analysis, only one of each set of similar attributes should be employed. The formula and numerical algorithms for computing these spatial attributes are listed in a series of tables below. The derived attributes are included in the feature attribute table of the object polygon representations. As the attribute values are calculated by aggregating all cells within an object, a significant increase in the signal-to-noise ratio has been achieved in comparison with the attribute value of a single cell. Therefore, object-based volumetric analysis is also more robust and reliable than the cell-by-cell differencing method. These computationally derived attributes provide comprehensive quantitative information to support a more detailed and reliable volumetric analysis of morphological changes. This represents a major advantage over the conventional cell-based method.

5.1. Planimetric attributes

The planimetric attributes describe the geographical position, horizontal dimensions, and size of the erosion and deposition objects. Those include the coordinates (x_c, y_c) of centroid point, perimeter (p), area (A), maximum distance to boundary (MDB), length (l) and width (w) of the minimum bounding rectangle. The numerical definitions of these attributes are listed in Table 1. The maximum distance to boundary is the radius of the largest circle that can be drawn within each object without including any cells outside the object. We adopt the algorithm in Suesse and Voss (2001) and Chaudhuri and Samal (2007) to compute the minimum bounding rectangle for each object, which is aligned along the major and minor principal axes of the object and contains all cells of the object. The length and width of the fitted minimum bounding rectangle indicate the horizontal dimensions of the object (Figure 2).

Table 1. Definitions of planimetric attributes.

Attributes	Definition
Centroid point (x_c, y_c)	$x_c = \frac{1}{n} \sum_{i=1}^n x(i); \quad y_c = \frac{1}{n} \sum_{i=1}^n y(i)$ <p>n is the number of cells consisting of an object, (x_i, y_i) are the horizontal and vertical coordinates of the ith cell of the object</p>
Perimeter (p)	$p = m_1 r + \sqrt{2} m_2 r$ <p>m_2 is the number of boundary cell in diagonal step, m_1 is the number of boundary cell in horizontal or vertical orientation, and r is the grid cell size</p>
Area (A)	$A = nr^2$ <p>n is the number of cells consisting of an object, and r is the grid cell size.</p>
Maximum distance to boundary (MDB)	$MDB = \max \{d_i\}$ <p>d_i is the distance of cell i to the nearest boundary.</p>
Length (l)	length of the minimum bounding rectangle enclosing the object
Width (w)	width of the minimum bounding rectangle enclosing the object

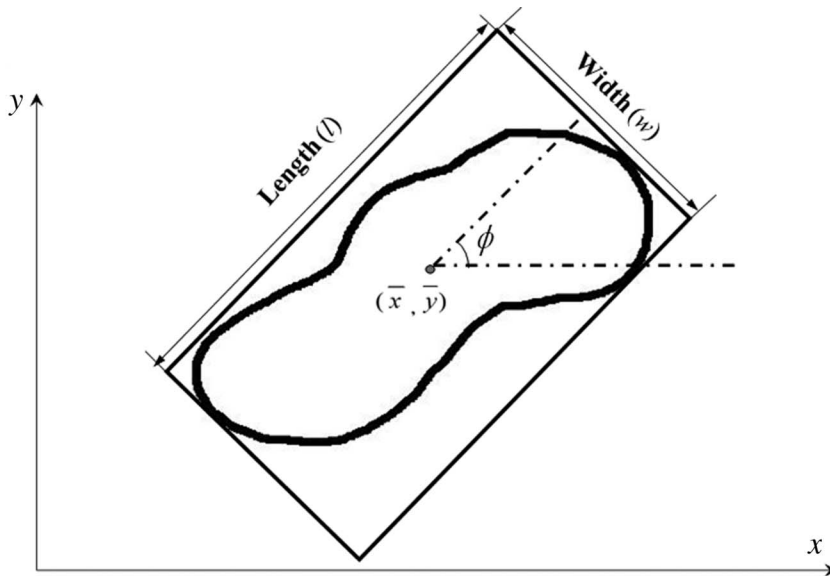


Figure 2. A minimum bounding rectangle and its parameters.

5.2. Shape attributes

This group of attributes is intended to capture the characteristics of the planar geometric shape of the objects. Owing to the differences in the nature of morphological changes and diverse coastal processes, the erosion and deposition objects may have different shape characteristics and complexity. Some may have compact forms, while others may exhibit distinctive narrow and elongated shapes. Some may have simple, regular, and smooth boundaries, while others may have convoluted, rugged, and complex fringes. Different types of erosion and deposition objects may be distinguished through the analysis of their shape characteristics. The significant differences in shape properties of erosion and deposition objects may provide diagnostic clues to the underlying coastal processes.

Owing to the infinite number of possible shapes, it is extremely difficult to quantitatively capture and measure the shape characteristics with a single attribute. In order to offer a comprehensive shape description, we compute a set of attributes for describing different aspects of the shape property. Those include compactness index (*CI*), elongatedness (*ELG*), asymmetry (*ASM*), orientation (ϕ), fractal dimension (*D*), rectangularity (*REC*), ellipticity (*ELP*), and triangularity (*TRI*) (Table 2). Most of these are dimensionless measures so that similar shapes should yield similar attribute values regardless of the size or orientation of the objects.

The compactness index (*CI*) is a widely used shape indicator (Davis 2002) defined by the perimeter and area of the object. The most compact object in a Euclidean space is a circle. A circle-shaped object has a compactness index of unity. The compactness index is also known as the circularity measure (Pratt 1991). Elongatedness (*ELG*) is defined as the ratio between the length and width of the fitted minimum bounding rectangle. A circle and square will have the smallest value for elongatedness.

Asymmetry and orientation are defined based on the best-fit ellipse of the object. The ellipse fitting can be performed based on the boundary cells using a least-squares approach (Rosin 1993, Fitzgibbon *et al.* 1999, Wynn and Stewart 2005) or based on all the cells within the object using low-order central moments of the object (Teague 1980, Mulchrone and

Table 2. Definitions of shape attributes.

Attributes	Definition
Compactness index (<i>CI</i>)	$CI = \frac{4\pi A}{P^2}$
Elongatedness (<i>ELG</i>)	$ELG = \frac{l}{w}$ l and w are the length and width of the minimum bounding rectangle.
Asymmetry (<i>ASM</i>)	$ASM = 1 - \frac{b}{a}$ $a = \sqrt{\frac{2(\mu_{20} + \mu_{02} + \sqrt{(\mu_{20} - \mu_{02})^2 + 4\mu_{11}^2})}{\mu_{00}}}$ $b = \sqrt{\frac{2(\mu_{20} + \mu_{02} - \sqrt{(\mu_{20} - \mu_{02})^2 + 4\mu_{11}^2})}{\mu_{00}}}$ $\mu_{pq} = \sum_{i=1}^n (x_i - \bar{x})^p (y_i - \bar{y})^q$ a and b are the semi-major and semi-minor of the best-fit ellipse, μ_{pq} are the central moments
Orientation (ϕ)	$\phi = \frac{1}{2} \tan^{-1} \left(\frac{2\mu_{11}}{\mu_{20} - \mu_{02}} \right)$ μ_{pq} are the central moments, ϕ is defined as an angle in degree between the x -axis and the major axis of the best-fit ellipse measured counterclockwise $[0, 180^\circ]$.
Fractal dimension (<i>D</i>)	$N(r) = cr^{1-D}$ r is the width of box, $N(r)$ is the counts of the boxes contain the object.
Rectangularity (<i>REC</i>)	$REC = \frac{A}{lw}$ A is the area of the object, and l and w are the length and width of the minimum bounding rectangle.
Ellipticity (<i>ELP</i>)	$ELP = \begin{cases} 16\pi^2 I_1 & \text{if } I_1 \leq 1/16\pi^2 \\ \frac{1}{16\pi^2 I_1} & \text{otherwise} \end{cases}$ $I_1 = \frac{\mu_{20}\mu_{02} - \mu_{11}^2}{\mu_{00}^2}$ μ_{pq} are the central moments and I_1 is the affine moment invariant.
Triangularity (<i>TRI</i>)	$TRI = \begin{cases} 108 I_1 & \text{if } I_1 \leq 1/108 \\ \frac{1}{108 I_1} & \text{otherwise} \end{cases}$ I_1 is the affine moment invariant.

Choudhury 2004). We adopt the latter approach so that the fitted ellipse is less affected by boundary irregularities of the object (Figure 3). The best-fit ellipse is located at the centroid of the object. The orientation of the maximum object spread is described by the angle in degree between the x -axis and the major principal axis of the ellipse measured counterclockwise with the possible range from 0° to 180° . The three parameters of the best-fit ellipse, namely, the semi-major axis (a), semi-minor axis (b), and the orientation (ϕ), are computed through the central moments of the objects (Teague 1980, Mulchrone and Choudhury 2004) as indicated in Table 2. The asymmetry (*ASM*) is defined as the ratio of the major and minor axes of the ellipse, which is the same as the ratio of the square roots of their eigenvalues. The circle and square have a value of 0 for asymmetry. The lengthier an object, the more asymmetric it is.

The shape complexity (smoothness) of object boundary can be measured in terms of a perimeter-to-area ratio or fractal dimension (Burrough 1981, Mandelbrot 1983). The more complex (less smooth) the boundary of an object is, the larger the perimeter-to-area ratio and fractal dimension are. The problem with the perimeter–area ratio as a shape attribute is that it varies with the size of the object. For two objects of the same level of shape complexity, the larger object has a smaller perimeter–area ratio than that of the smaller object. To avoid the

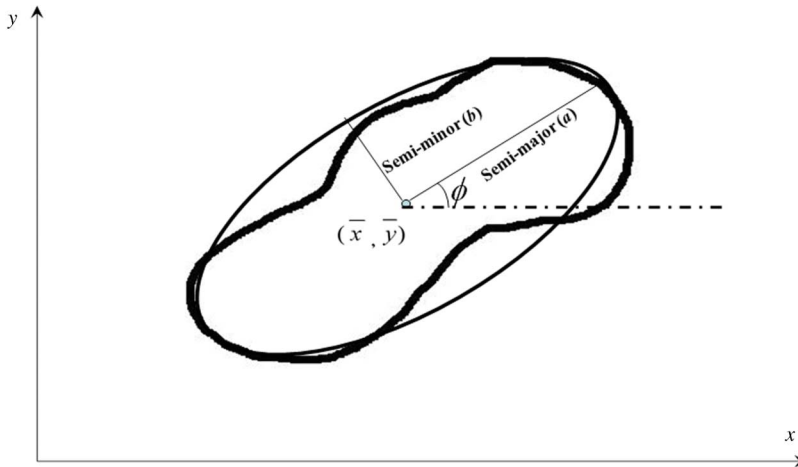


Figure 3. Best-fit ellipse and its parameters.

size dependency problem, we select the fractal dimension to measure the complexity (smoothness) of object boundary. The computation of fractal dimension is implemented using the box-counting method (Foroutan-pour *et al.* 1999). Within the Feret box (the smallest rectangle oriented with respect to the coordinate axis that bounds the object), the original cells of the object are successively merged into larger square boxes with an increasing width (r). At each merging level, which is indicated by the width (r) of the square boxes, the number $N(r)$ of boxes that contain at least a portion (whatever small) of the object is counted. The fractal dimension for each object is determined by the slope of the regression line of $\log(N(r))$ on $\log(r)$.

Rectangularity, ellipticity, and triangularity measure the similarity of the object to a typical rectangle, ellipse, or triangle shape. Rectangularity is defined by the comparison of the area of the object with the area of the minimum bounding rectangle. The ellipticity and triangularity are defined based on the affine moment invariant (Flusser and Suk 1993, Rosin 2003). Their values range from 0 to 1.0, and larger values indicate greater similarity to the corresponding typical shape.

5.3. Surface attributes

The three-dimensional surface morphology and its changes can be captured and measured in terms of surface slope, aspect, and curvature. Surface geomorphology strongly reflects various coastal processes in the patterns of erosion and deposition, and may feed back to influence coastal processes. For example, surface slope of the beach is a consequence of the interplay of sediment grain size and nearshore energy environment. Backshore slopes may interact with eolian processes to enhance or inhibit rates of blowing sand transport (Sherman and Bauer 1993) and alter characteristics of wind flow (Hesp *et al.* 2005). Surface aspect will determine the directions from which winds and waves might do the most (or least) work (Bauer and Davidson-Arnott 2003). Surface curvature is a measure of convexity or concavity, and in the context of beach profile configuration, may provide fundamental morphodynamic information (Wright and Short 1984).

To support the exploration of the relationships between surface properties and erosion and deposition patterns, we compute a set of surface attributes for each erosion and deposition

Table 3. Definitions of surface attributes.

Attributes	Definition
Original-surface average elevation (AV_EL_1)	$AV_EL_1 = \frac{1}{n} \sum_{i=1}^n z_i^{t1}$
Subsequent-surface average elevation (AV_EL_2)	$AV_EL_2 = \frac{1}{n} \sum_{i=1}^n z_i^{t2}$
Average elevation difference (AV_EL_DIF)	$AV_EL_DIF = AV_EL_2 - AV_EL_1$ z_i^{t1} and z_i^{t2} are the elevations of cell i of the object respectively at time $t1$ and $t2$
Original-surface average slope (AV_SL_1)	$AV_SL_1 = \frac{1}{n} \sum_{i=1}^n s_i^{t1}$
Subsequent-surface average slope (AV_SL_2)	$AV_SL_2 = \frac{1}{n} \sum_{i=1}^n s_i^{t2}$
Average slope difference (AV_SL_DIF)	$AV_SL_DIF = AV_SL_2 - AV_SL_1$ s_i^{t1} and s_i^{t2} are the surface slopes of cell i of the object respectively at time $t1$ and $t2$
Original-surface average aspect (AV_AP_1)	$AV_AP_1 = \tan^{-1} \left(\frac{\sum_{i=1}^n \sin \theta_i^{t1}}{\sum_{i=1}^n \cos \theta_i^{t1}} \right)$
Subsequent-surface average aspect (AV_AP_2)	$AV_AP_2 = \tan^{-1} \left(\frac{\sum_{i=1}^n \sin \theta_i^{t2}}{\sum_{i=1}^n \cos \theta_i^{t2}} \right)$
Average aspect difference (AV_AP_DIF)	$AV_AP_DIF = AV_AP_2 - AV_AP_1$ θ_i^{t1} and θ_i^{t2} are the surface aspects of cell i of the object respectively at time $t1$ and $t2$
Original-surface average curvature (AV_CV_1)	$AV_CV_1 = \frac{1}{n} \sum_{i=1}^n v_i^{t1}$
Subsequent-surface average curvature (AV_CV_2)	$AV_CV_2 = \frac{1}{n} \sum_{i=1}^n v_i^{t2}$
Average curvature difference (AV_CV_DIF)	$AV_CV_DIF = AV_CV_2 - AV_CV_1$ v_i^{t1} and v_i^{t2} are the surface aspects of cell i of the object respectively at time $t1$ and $t2$

object. Those include original-surface average elevation (AV_EL_1), subsequent-surface average elevation (AV_EL_2), average elevation difference (AV_EL_DIF), original-surface average slope (AV_SL_1), subsequent-surface average slope (AV_SL_2), average surface slope difference (AV_SL_DIF), original-surface average aspect (AV_AS_1), subsequent-surface average aspect (AV_AS_2), average surface aspect difference (AV_AS_DIF), original-surface curvature (AV_CV_1), subsequent-surface curvature (AV_CV_2), and average surface curvature difference (AV_CV_DIF) (Table 3). The average value of surface elevation, slope (in percent rise), or curvature for original and subsequent surfaces are simply calculated as the arithmetic mean of all the cells within the object. The average value for surface aspect is calculated through trigonometric operations as it is a circular direction measure in degree (Davis 2002).

5.4. Volumetric attributes

The volumetric attributes give direct measurements on the magnitude and rate of sediment erosion and deposition. Attributes in this category include average vertical change (Δz_{av}), maximum vertical change (Δz_{max}), standard deviation of vertical change (Δz_{std}), vertical

Table 4. Definitions of volumetric attributes.

Attributes	Definition
Average vertical change (ΔZ_{av})	$\Delta Z_{av} = \frac{1}{n} \sum_{i=1}^n \Delta Z_i$ $\Delta Z_i \text{ is the elevation change of cell } i \text{ of the object.}$
Maximum vertical change (ΔZ_{max})	$\Delta Z_{max} = \max\{\Delta Z_i\}$
Standard deviation of vertical changes (ΔZ_{std})	$\Delta Z_{std} = \frac{1}{n-1} \sqrt{\sum_{i=1}^n (\Delta Z_i - \Delta Z_{av})^2}$
Vertical change rate (ZR)	$ZR = \frac{\Delta Z_{av}}{\Delta t}$ $\Delta t \text{ is the elapsed time between two consecutive topography surveys } (t2-t1)$
Volume change (VOL)	$VOL = r^2 \sum_{i=1}^n \Delta Z_i$
Volume change rate (VR)	$VR = \frac{VOL}{\Delta t}$

change rate (ZR), volume (VOL), and volume rate (VR) (Table 4). The average vertical change (Δz_{av}) is the mean of erosion or deposition depth of all grid cells inside each object, and vertical change rate (ZR) is the annual (or other relevant time interval) average erosion or deposition depth. Maximum vertical change (Δz_{max}) indicates the largest erosion or deposition depth within the object. The standard deviation of vertical change (Δz_{std}) gauges the variation of erosion or deposition depth of grid cells within each object. The volume (VOL) quantifies the total erosion or deposition volume (in cubic meters) during the time span between two successive surveys, and volume rate (VR) gives annual erosion or deposition volume for each object.

5.5. Summary statistical attributes

The attributes are calculated for each individual erosion or deposition object. Summary statistics are computed to quantify the extent, amount, spatial composition, and configuration of overall erosion, deposition, and net change based on all objects over the entire scene under investigation. The attributes in this category include the number of erosion objects (NUM_ER), average size of erosion objects (AV_AREA_ER), total erosion area ($AREA_ER$), total erosion volume (VOL_ER), the number of deposition objects (NUM_DE), average size of deposition objects (AV_AREA_DE), total deposition area ($AREA_DE$), total deposition volume (VOL_DE), net volume change (NET_VOL), and annual net volume change rate (NET_VOL_RT) (Table 5).

The attributes of different categories provide comprehensive quantitative information for various aspects of coastal morphology. The attribute information is essential for improving computational modeling and prediction of coastal morphological changes and for gaining insights into the underlying coastal processes that shape and modify coastal morphology. Coastal processes influencing coastal geomorphology include human activities (construction and demolition of buildings and flood defense structures, nourishments, movement of vehicles, etc.); sedimentation induced by waves, storms and winds; and vegetation dynamics (growths and seasonal changes). Since pattern and process are intimately related, the analysis of pattern also provides a key to understanding coastal morphological dynamics. The morphological changes caused by vegetation dynamics, winds, and waves have different spatial characteristics that may be reflected by distinct attribute values. The quantitative

Table 5. Definitions of summary statistical attributes.

Attributes	Definition
Number of erosion objects (<i>NUM_ER</i>)	<i>NUM_ER</i> = Number of erosion objects
Number of deposition objects (<i>NUM_DE</i>)	<i>NUM_DE</i> = Number of deposition objects
Total erosion area (<i>AREA_ER</i>)	$AREA_ER = \sum_{j=1}^{NUM_ER} A_j^e$
Total deposition area (<i>AREA_DE</i>)	$AREA_DE = \sum_{j=1}^{NUM_DE} A_j^d$ <p>A_j^e is the areal change of the <i>j</i>th erosion object. A_j^d is the areal change of the <i>j</i>th deposition object</p>
Average size of erosion object (<i>AV_AREA_ER</i>)	$AV_AREA_ER = \frac{1}{NUM_ER} \sum_{j=1}^{NUM_ER} A_j^e$
Average size of deposition object (<i>AV_AREA_DE</i>)	$AV_AREA_DE = \frac{1}{NUM_DE} \sum_{j=1}^{NUM_DE} A_j^d$
Total erosion volume (<i>VOL_ER</i>)	$VOL_ER = \sum_{j=1}^{n1} VOL_j^e$
Total deposition volume (<i>VOL_DE</i>)	$VOL_DE = \sum_{j=1}^{NUM_DE} VOL_j^d$ <p>VOL_j^e is the volume change of the <i>j</i>th erosion object. VOL_j^d is the volume change of the <i>j</i>th deposition object.</p>
Net volume change	$NET_VOL = VOL_DE - VOL_ER$
Net volume change rate (<i>NET_VOL_RT</i>)	$NET_VOL_RT = NET_VOL / \Delta t$

analysis of attribute values renders the capability of discriminating and classifying individual change objects into different classes to pursue a better understanding of the nature and characteristics of morphological changes for each class. The object-based quantitative information about erosion and deposition patches and zones also offers a more detailed and reliable assessment of the damaging impacts of events like storms and hurricanes and the effects of human interventions like beach nourishments and constructions of groins, jetties, geotubes, and other coastal defense structures. This will provide a scientific basis for formulating appropriate planning and management strategies and measures for protecting the coastal areas.

6. Implementation of object-based morphological analysis software tool

We have developed numerical algorithms for erosion and deposition object delineation and their attribute derivation to support object-based morphological analysis. Considering the widespread use of ArcGIS software in geospatial and coastal research communities, our analysis tool is implemented as an ArcGIS extension module – Coastal Morphology Analyst, which will be freely available for the public to download through the internet.

The core algorithm components are programmed as a series of Dynamic Link Library (DLL) using the language C++. The graphical interface for the Coastal Morphology Analyst extension module is accomplished through VB.NET programs that call and wrap our specialized DLLs and the relevant ArcObjects. The ArcObjects are a set of platform-independent software components designed by ESRI, Inc. specifically for developing ArcGIS applications. Our extension module can be installed with a user-friendly setup procedure and used seamlessly with ArcGIS package.

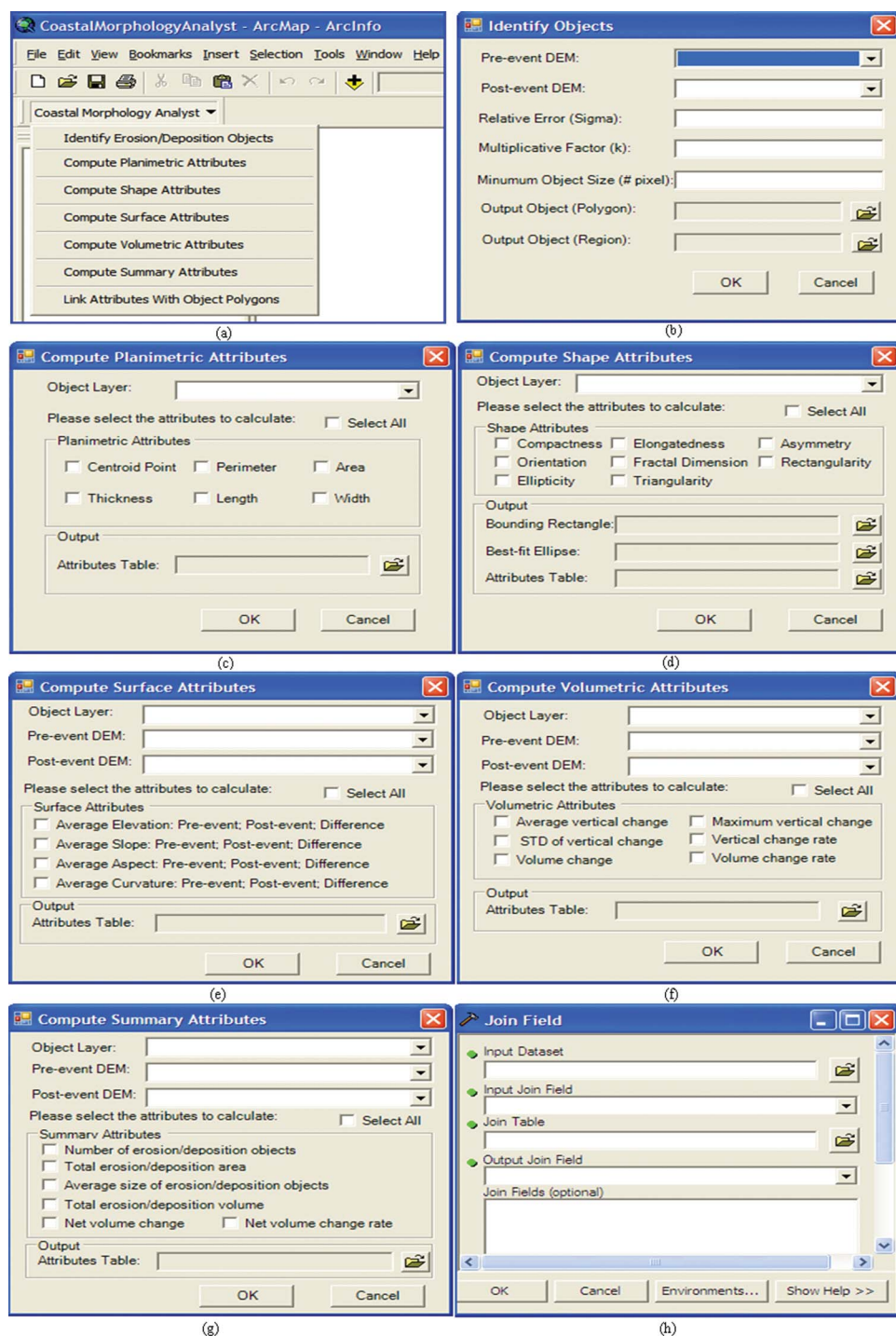


Figure 4. ArcGIS extension module – Coastal Morphology Analyst. (a) Pull-down menu for the extension module; (b) dialogue form for identifying erosion and deposition objects; (c) dialogue form for computing planimetric attributes; (d) dialogue form for computing shape attributes; (e) dialogue form for computing surface attributes; (f) dialogue form for computing volumetric attributes; (g) dialogue form for computing summary statistical attributes; and (h) dialogue form for linking attribute tables with object polygon coverage.

The graphical interface for Coastal Morphology Analyst is shown in Figure 4a. This pull-down menu contains seven command tools. Each command tool is implemented as a customized dialogue menu guiding the user to load input data, to set relevant parameter values, and to specify output products. The first command tool (Figure 4b) aims to identify erosion and deposition objects. The input data sets to be loaded are two sequential LiDAR DEMs, which are acquired at different times and cover the same area. The original DEM is specified as pre-event surface and the subsequent DEM as post-event terrain surface. As discussed above, these two DEMs must have the same map projection and be referenced to the same vertical datum. Besides the input DEMs, the user needs to set three additional parameters: the relative error σ_d (with a default value of 0.2 m), multiplicative factor k (with a default value of 2.0), and the minimum object size in the number of grid cells (with a default value of 1 cell) to remove small noisy objects. The output objects are given in two formats: polygon vector shape files and raster regions (zones). In the raster representation, each object is designated by its constituent grid cells with the same integer ID number, and the object attributes are stored in an associated value attribute table (VAT). In the vector representation, each object is represented by a polygon as its boundary, and a feature attribute table is associated with the vector polygon geometry. The dual raster–vector representation of extracted erosion/deposition objects facilitates the modularity and flexibility of subsequent attribute computation. By default a specialized renderer method is applied to highlight erosion and deposition objects. The five categories of attributes can be computed by subsequent command tools. As shown in Figure 4c–g, the user can select specific attributes to be computed and included for each category. For the command tool that calculates shape attributes, the user can select to output the minimum bounding rectangles and the best-fit ellipses for erosion and deposition objects as two separate polygon data sets (Figure 4d). The last command tool (Figure 4h) is used to link and join the computed attribute tables with the object polygons.

Embedding the object-based morphological analysis into ArcGIS as an extension module has several advantages. It allows users to utilize the powerful ArcGIS functions in data management, visualization, and spatial analysis. The input LiDAR DEMs in ArcGIS-compatible format can be directly loaded and used in the morphology analysis module. Intermediate processing results can be displayed immediately and checked using a variety of ArcGIS visualization functions. It is convenient to compare and integrate the erosion and deposition polygon shape files from the morphological analysis with other GIS data layers for map composition and further numerical analysis and modeling.

It should be noted that our software tool, Coastal Morphology Analyst, is significantly different from the landscape ecology software tool FRAGSTATS (McGarigal and Marks 1995, McGarigal *et al.* 2002), which does not have the function to create meaningful objects (patches). While the metrics (attributes) computed in FRAGSTATS focus on the descriptions of two-dimensional geometric properties and ecological functions, our ArcGIS Coastal Morphology Analyst module is dedicated for the coastal morphological change analysis, computing additional shape attributes, three-dimensional surface attributes, and volumetric attributes.

7. An application example for volumetric estimates

An application example is given to illustrate the data-processing procedures and utility of our method. Our case study area is part of Assateague Island, MD, USA (Figure 5). Assateague Island is a highly dynamic place, as currents, winds, and storms continuously reshape the coast.

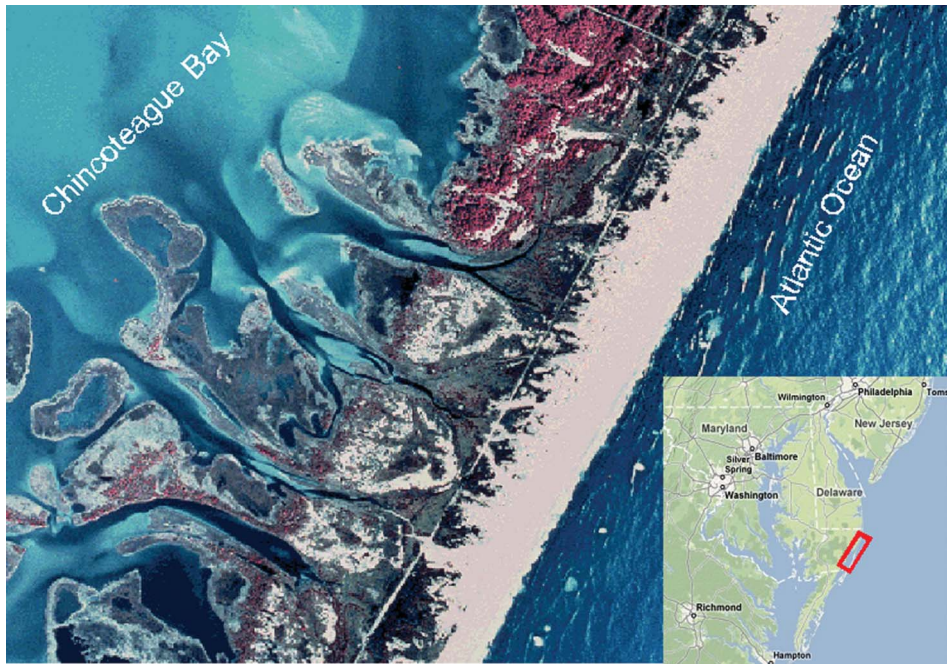


Figure 5. The geographical settings of Whittington Point of Assateague Island, MD, USA, as shown in a color-infrared aerial photograph.

Our volumetric change analysis is conducted for a 1.85 km stretch of the island around Whittington Point. This area includes shoreline, beaches, foredunes, highway, shrubs, pine forest, brackish-water marshes, tidal flats, and other natural features (Figure 5). The two LiDAR surveys used in this analysis were acquired by NASA's Airborne Topographic Mapper (ATM) LiDAR system. The first survey was conducted on 15 September 1997, and the second one was on 20 September 2000. Raw elevation measurements have been determined to be vertically accurate to within 0.15 m and horizontally accurate to 0.8 m. The LiDAR measurements are spatially interpolated into two DEMs grids at 1 m spatial resolution. The LiDAR DEMs are projected to the UTM (zone 18) coordinate system, horizontally referenced to WGS84 ellipsoid. The elevation values are referenced to the orthometric North American Vertical Datum of 1988 (NAVD88). As shown in the gray-scale (Figure 6a and b) and hill-shaded LiDAR images (Figure 9), subtle and micromorphological features such as beaches, dunes, roads, and vegetation can be resolved and recognized owing to high spatial resolution and vertical accuracy of the LiDAR measurements.

The change (difference) grid is created by subtracting the 1997 LiDAR grid from the 2000 LiDAR grid (Figure 6c). The relative error (σ_d) of the change values is estimated to be 0.21 m based on the vertical accuracy of 0.15 m. By taking $k = 2.0$, we have identified and delineated erosion and deposition objects as shown (Figure 7a). Subsequently, we have computed several selected attributes for these objects, including size, fractal dimension, average vertical change, and standard deviation of vertical changes. The initial set of erosion and deposition objects include many change patches induced by vegetation dynamics as well as spurious change patches near the shoreline caused by waves and run-up, whereas our focus is on sediment-induced morphological and volumetric changes in the beach and dune zones. We observed that vegetation dynamics-induced change patches commonly have

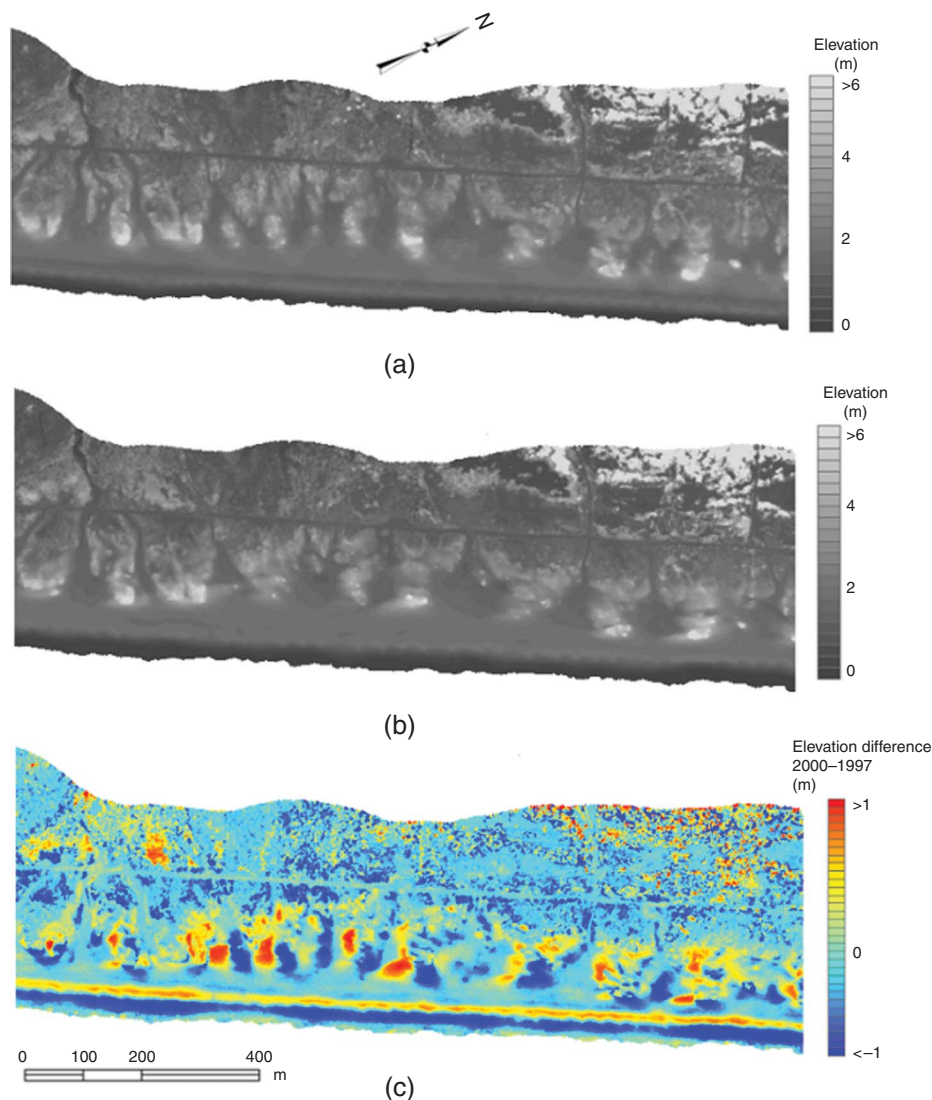


Figure 6. LiDAR DEMs and the elevation difference grid. (a) Original surface DEM acquired in 1997; (b) subsequent surface DEM acquired in 2000; and (c) cell-by-cell elevation changes during 1997–2000.

irregular and rough boundaries as well as many holes and gaps, and therefore have a large fractal dimension. Furthermore, the vertical variation inside vegetation patches is much larger and more discontinuous than that associated with sediment surfaces. The spurious change patches caused by waves and run-up generally have a small size. Based on these observations, we remove the patches induced by vegetation dynamics, waves and run-up, and other data noise by filtering objects whose fractal dimension is $(D) > 1.4$, or size is $(A) < 190 \text{ m}^2$, or the standard deviation of vertical changes is $(\Delta z_{\text{std}}) > 0.6 \text{ m}$. Several large positive change patches in the upper left part of Figure 7a are caused by vegetation changes, which were confirmed by using a color-infrared aerial photograph. These objects have relatively high fractal dimensions and large vertical elevation changes and are excluded for further analysis of sediment erosion and deposition. The other remaining objects

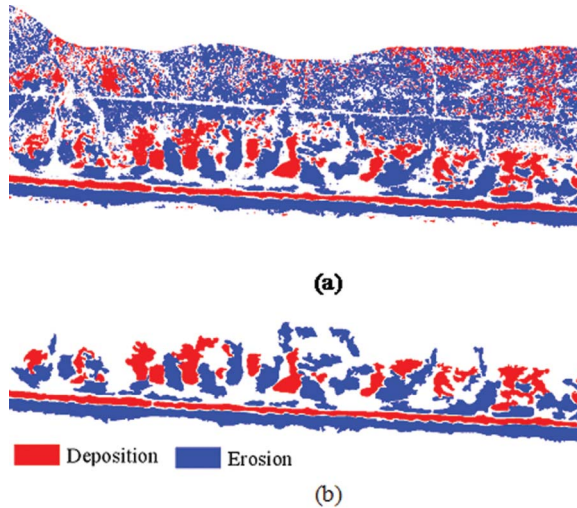


Figure 7. Erosion and deposition objects. (a) Original objects detected by using $\sigma_d = 0.21$ m and $k = 2.0$; (b) after removing spurious objects induced by vegetation dynamics and waves and run-up.

(Figure 7b) are considered to be erosion and deposition objects induced by sediment transport. We applied morphological operations to smooth the remaining objects and then computed all the planimetric, shape, surface, and volumetric attributes as well as summary statistical attributes for the objects. The minimum bounding rectangles and best-fit ellipses have also been created for all erosion and deposition objects. The fitted rectangles and ellipses are shown only for a part of the study area in Figure 8. The computed attribute values are listed in Table 6 for the objects depicted in Figure 8. The erosion and deposition polygons are also overlain on the top of the hill-shaded relief images to explore the relationship of erosion and deposition pattern to the coastal morphology. The total erosion, deposition, and net volume change are normalized by dividing these values by the corresponding shoreline length.

The results indicate severe erosion along the beach zone. A continuous, long erosion zone (Object 563) (Figure 9 and Table 6) is oriented along the shoreline with an azimuth angle of 62° from the true north. This elongated erosion zone has a largest width of 35.70 m and an average erosion depth of 0.73 m. The average elevation of this zone has been reduced from 1.09 to 0.37 m. The total erosion volume was $10,064 \text{ m}^3$ during 1997–2000, and the normalized erosion volume rate is 5.45 m^3 per meter of shoreline stretch. Erosion processes have modified the beach from its slightly convex downward shape (curvature of 0.56) in 1997 to a concave upward shape (curvature of -0.97) in 2000. There is landward berm migration (Figure 9). In addition, there was a long depression feature in the back beach, which can be recognized in the 1997 hill-shaded relief image (Figure 9a). The depression was almost filled by sediment in 2000 (Figure 9b), causing a narrow deposition zone (Object 571) along the back beach. This zone has a maximum width of 16.40 m and an average deposition thickness of 0.47 m. The concave surface curvature (-1.40) along the depression disappeared by 2000. Both erosion and deposition objects in the beach zone have elongated and asymmetric shapes and are oriented parallel to the shoreline (Table 6).

Significant morphological changes in the dune zone can be observed by comparing the 1997 and 2000 hill-shaded relief images of the LiDAR data (Figure 9a and b). The dune migration in the southwest direction is apparent. Plume-like features can be observed in the

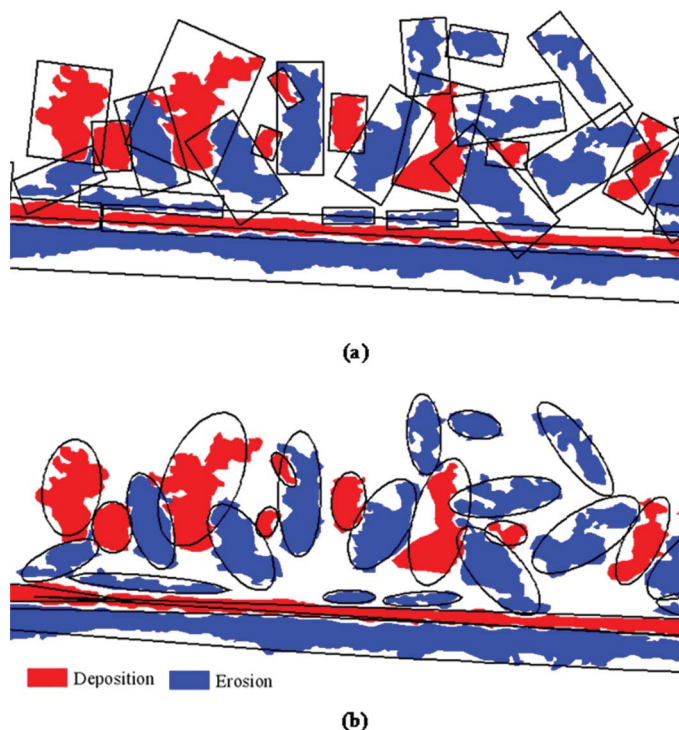


Figure 8. Fitted rectangles and ellipses for erosion and deposition objects. (a) Minimum bounding rectangles; (b) best-fit ellipses.

south side of many dunes in the 2000 hill-shaded relief image (Figure 9b). The significant dune movement is most likely caused by the northeast winds. These winds erode and transport sand from the dune's upwind side and deposit on the leeward side of the dunes, causing downwind dune migration. Local redistribution of sand has produced many discrete erosion and deposition patches in the dune zone (Figure 9). As expected, erosion patches occurred on the upwind side of dunes, and deposition patches are located on the leeward side of dunes (Figure 9a). The erosion patches are interspersed with deposition patches. The position and shape of many dunes were changed considerably by erosion and deposition processes. Some sand dunes (e.g. Object 461) were destroyed by erosion. The spatial patterns of erosion and deposition zones in the dune zone contrast with that of the beach. In general, erosion and deposition zones in the dunes have irregular and complex boundaries, compared with the elongated erosion and deposition zones in the beach. Most erosion and deposition zones in the dunes have a more compact shape and are oriented approximately perpendicular to the shoreline. The surface shape of all erosion patches has been changed from convex to concave (Table 6). The opposite is true for all the deposition patches. In the dune zone, the average depth of erosion patches reaches 0.85 m (Object 461), and the average thickness of the deposition patches can be as large as 0.91 m (Object 494). Since no washover deposition patches are recognized in the interdune swales or tidal channels in the bayside, we believe that no storm-induced washover events occurred during 1997–2000.

For the 1.85-km-coastal stretch of our study area, we detected 34 erosion objects and 23 deposition objects. The total erosion area is 109,506 m², and the total erosion volume is estimated to be 66,594 m³. The total deposition area is 54,699 m², and the total deposition

Table 6. Derived attribute values for erosion and deposition objects.

ID	Type	x_c (m)	y_c (m)	p (m)	A (m ²)	MDB (m)	l (m)	w (m)	CI	ELG	ASM	ϕ
461	Erosion	481,383	4,212,770	272	2684	16.9	95.0	39.2	0.46	2.42	0.59	170.5
486	Erosion	481,469	4,212,750	337	2826	16.4	94.0	46.0	0.31	2.04	0.51	7.7
563	Erosion	481,774	4,212,650	3683	41,549	19.7	1847.0	35.7	0.04	51.68	0.98	62.1
510	Erosion	481,712	4,212,720	391	3062	20.5	107.7	45.4	0.25	2.37	0.58	16.9
409	Erosion	481,527	4,212,790	343	2938	17.0	120.6	41.1	0.31	2.94	0.66	154.4
445	Erosion	481,924	4,212,750	794	5838	23.5	188.3	60.4	0.12	3.12	0.68	98.3
464	Erosion	481,607	4,212,770	344	2896	17.7	96.7	48.5	0.31	1.99	0.50	123.5
378	Erosion	481,789	4,212,840	402	1824	8.8	111.3	32.3	0.14	3.45	0.71	12.6
457	Erosion	481,725	4,212,800	393	2190	8.7	107.7	36.3	0.18	2.97	0.66	73.2
376	Erosion	481,693	4,212,870	153	895	6.4	50.5	25.7	0.48	1.96	0.49	54.4
358	Erosion	481,646	4,212,850	323	1424	9.2	77.4	32.4	0.17	2.39	0.58	158.5
526	Erosion	481,299	4,212,740	286	1344	10.5	79.7	28.5	0.21	2.80	0.64	88.4
495	Erosion	481,795	4,212,750	407	3053	14.5	117.3	47.9	0.23	2.45	0.59	97.3
550	Erosion	481,376	4,212,710	330	1220	6.7	153.6	14.8	0.14	10.39	0.90	60.3
565	Erosion	481,575	4,212,700	112	449	5.5	50.2	12.7	0.45	3.96	0.75	65.2
570	Erosion	481,922	4,212,690	329	1544	8.4	115.2	24.8	0.18	4.65	0.78	58.4
568	Erosion	481,645	4,212,700	174	587	4.5	75.4	13.4	0.24	5.65	0.82	67.3
502	Deposition	481,493	4,212,770	90	365	6.9	29.7	19.4	0.57	1.53	0.35	135.7
518	Deposition	481,725	4,212,760	117	493	5.7	40.5	23.3	0.45	1.74	0.42	58.0
424	Deposition	481,509	4,212,820	94	357	7.4	37.2	15.4	0.51	2.41	0.59	5.9
474	Deposition	481,925	4,212,780	245	1733	10.2	73.4	38.6	0.36	1.90	0.47	81.0
488	Deposition	481,853	4,212,750	272	1863	13.4	92.9	34.5	0.32	2.70	0.63	128.2
571	Deposition	481,923	4,212,670	2484	14,699	9.5	1329.2	16.4	0.03	81.20	0.99	62.2
547	Deposition	481,156	4,212,710	790	5684	10.7	434.0	19.0	0.11	22.86	0.96	61.2
414	Deposition	481,308	4,212,800	361	3297	13.4	92.6	55.7	0.32	1.66	0.40	147.8
393	Deposition	481,430	4,212,800	668	4633	17.7	136.3	70.6	0.13	1.93	0.48	131.4
443	Deposition	481,657	4,212,760	371	3151	18.5	124.4	52.3	0.29	2.38	0.58	140.8
462	Deposition	481,570	4,212,790	186	1298	13.4	55.4	32.6	0.47	1.70	0.41	150.5
494	Deposition	481,346	4,212,770	154	1407	16.4	48.9	38.0	0.75	1.29	0.22	157.3

(Continued)

Table 6. (Continued)

ID	Type	D	REC	ELP	TRI	AV_EL ₁	AV_EL ₂	AV_EL_DIF	AV_SL ₁	AV_SL ₂	AV_SL_DIF	AV_AP ₁
461	Erosion	1.124	0.72	0.84	0.81	2.78	1.93	-0.85	6.66	3.25	-3.41	169.5
486	Erosion	1.181	0.65	0.69	0.99	3.02	2.29	-0.73	5.20	2.88	-2.32	168.7
563	Erosion	1.187	0.63	0.64	0.94	1.09	0.37	-0.73	4.27	4.19	-0.08	180.4
510	Erosion	1.268	0.63	0.63	0.93	3.32	2.62	-0.70	5.55	3.93	-1.62	163.3
409	Erosion	1.175	0.59	0.57	0.83	2.17	1.54	-0.63	4.70	3.32	-1.38	164.1
445	Erosion	1.250	0.51	0.43	0.62	2.75	2.16	-0.59	5.01	3.86	-1.15	159.2
464	Erosion	1.230	0.62	0.62	0.90	2.75	2.18	-0.57	5.84	5.00	-0.83	155.8
378	Erosion	1.303	0.51	0.42	0.61	2.34	1.80	-0.54	8.18	6.63	-1.55	173.9
457	Erosion	1.334	0.56	0.51	0.74	2.48	2.06	-0.42	4.91	3.96	-0.96	147.7
376	Erosion	1.376	0.69	0.77	0.89	2.01	1.60	-0.41	8.02	5.94	-2.08	164.6
358	Erosion	1.258	0.57	0.52	0.76	1.65	1.26	-0.39	4.26	3.52	-0.75	173.5
526	Erosion	1.214	0.59	0.57	0.83	2.69	2.32	-0.37	4.75	4.53	-0.23	178.6
495	Erosion	1.247	0.54	0.48	0.70	1.93	1.58	-0.35	2.44	1.58	-0.86	157.2
550	Erosion	1.218	0.54	0.47	0.68	2.12	1.84	-0.28	1.17	1.23	0.06	180.3
565	Erosion	1.154	0.70	0.80	0.85	2.09	1.82	-0.28	0.91	1.15	0.24	182.4
570	Erosion	1.269	0.54	0.47	0.69	2.20	1.92	-0.28	0.91	1.20	0.29	177.1
568	Erosion	1.402	0.58	0.55	0.80	2.12	1.87	-0.24	0.79	1.11	0.31	152.8
502	Deposition	1.124	0.63	0.65	0.95	1.40	1.66	0.27	1.48	1.12	-0.35	154.6
518	Deposition	1.319	0.52	0.44	0.65	2.18	2.46	0.28	4.72	4.53	-0.19	86.6
424	Deposition	1.222	0.62	0.63	0.92	1.73	2.16	0.43	5.96	6.53	0.56	231.2
474	Deposition	1.236	0.61	0.61	0.89	2.71	3.15	0.45	5.73	5.04	-0.69	171.7
488	Deposition	1.126	0.58	0.55	0.80	1.94	2.39	0.45	3.65	3.94	0.29	258.4
571	Deposition	1.213	0.68	0.74	0.92	1.60	2.07	0.47	2.49	2.25	-0.24	174.5
547	Deposition	1.159	0.69	0.77	0.89	1.53	2.00	0.48	2.20	1.67	-0.54	173.7
414	Deposition	1.290	0.64	0.66	0.97	3.04	3.57	0.53	7.23	6.59	-0.63	199.3
393	Deposition	1.337	0.48	0.38	0.55	2.46	3.06	0.60	5.85	5.12	-0.72	182.9
443	Deposition	1.178	0.48	0.38	0.56	2.04	2.72	0.68	3.95	5.25	1.30	222.1
462	Deposition	1.141	0.72	0.84	0.81	2.14	2.97	0.84	6.46	7.62	1.16	264.0
494	Deposition	1.134	0.76	0.93	0.74	1.91	2.82	0.91	4.64	4.52	-0.12	157.8

ID	Type	AV_AP ₂	AV_AP_DIF	AV_CV ₁	AV_CV ₂	AV_CV_DIF	Δz_v (m)	Δz_{\max} (m)	Δz_{std} (m)	ZR (m/yr)	VOL (m ³)	VR (m ³ /yr)
461	Erosion	165.3	-4.2	1.13	-1.60	-2.72	-0.85	-2.80	0.55	-0.28	-2270.15	-756.72
486	Erosion	143.6	-25.1	0.91	-1.10	-2.01	-0.73	-3.24	0.56	-0.24	-2054.76	-684.92
563	Erosion	182.6	2.2	0.56	-0.97	-1.53	-0.73	-2.06	0.38	-0.24	-30193.50	-10064.50
510	Erosion	176.0	12.7	1.39	-1.74	-3.13	-0.70	-2.70	0.58	-0.23	-2151.90	-717.30
409	Erosion	153.6	-10.5	0.46	-1.63	-2.09	-0.63	-2.21	0.36	-0.21	-1851.95	-617.32
445	Erosion	154.5	-4.7	1.26	-1.04	-2.30	-0.59	-2.63	0.39	-0.20	-3432.81	-1144.27
464	Erosion	150.4	-5.4	0.95	-1.40	-2.35	-0.57	-1.80	0.31	-0.19	-1660.90	-553.63
378	Erosion	186.9	13.0	3.43	-2.85	-6.29	-0.54	-1.71	0.27	-0.18	-990.99	-330.33
457	Erosion	144.4	-3.3	2.08	-2.07	-4.15	-0.42	-1.23	0.17	-0.14	-910.20	-303.40
376	Erosion	156.9	-7.8	3.87	-1.70	-5.58	-0.41	-1.33	0.21	-0.14	-370.02	-123.34
358	Erosion	175.3	1.8	1.39	-2.22	-3.61	-0.39	-1.12	0.18	-0.13	-559.94	-186.65
526	Erosion	176.7	-1.9	2.02	-2.37	-4.39	-0.37	-1.70	0.20	-0.12	-496.89	-165.63
495	Erosion	152.7	-4.4	0.54	-1.05	-1.59	-0.35	-1.62	0.14	-0.12	-1068.50	-356.17
550	Erosion	181.8	1.5	1.16	-1.14	-2.30	-0.28	-0.46	0.05	-0.09	-341.47	-113.82
565	Erosion	198.5	16.1	1.34	-1.10	-2.45	-0.28	-0.39	0.05	-0.09	-124.61	-41.54
570	Erosion	185.9	8.9	0.73	-0.84	-1.58	-0.28	-0.44	0.05	-0.09	-427.00	-142.33
568	Erosion	178.1	25.3	1.02	-1.54	-2.56	-0.24	-0.35	0.03	-0.08	-143.11	-47.70
502	Deposition	119.1	-35.5	-1.47	0.54	2.01	0.27	0.38	0.05	0.09	96.80	32.27
518	Deposition	73.2	-13.4	-3.61	2.70	6.30	0.28	0.63	0.06	0.09	137.66	45.89
424	Deposition	252.5	21.3	-3.10	3.24	6.35	0.43	0.77	0.15	0.14	152.64	50.88
474	Deposition	182.2	10.4	-2.77	1.69	4.46	0.45	1.07	0.17	0.15	773.20	257.73
488	Deposition	261.0	2.5	-1.87	0.84	2.71	0.45	0.96	0.16	0.15	841.34	280.45
571	Deposition	178.8	4.3	-1.40	1.67	3.07	0.47	1.00	0.16	0.16	6943.01	2314.34
547	Deposition	170.3	-3.4	-1.01	1.13	2.14	0.48	0.93	0.16	0.16	2709.12	903.04
414	Deposition	207.9	8.5	-1.08	2.23	3.31	0.53	1.87	0.25	0.18	1736.17	578.72
393	Deposition	193.0	10.1	-2.55	1.72	4.26	0.60	1.69	0.37	0.20	2774.32	924.77
443	Deposition	249.9	27.8	-1.04	1.57	2.61	0.68	1.81	0.40	0.23	2146.26	715.42
462	Deposition	264.2	0.2	-1.38	2.21	3.59	0.84	2.00	0.49	0.28	1088.06	362.69
494	Deposition	143.3	-14.5	-3.55	0.33	3.88	0.91	1.71	0.44	0.30	1285.00	428.33

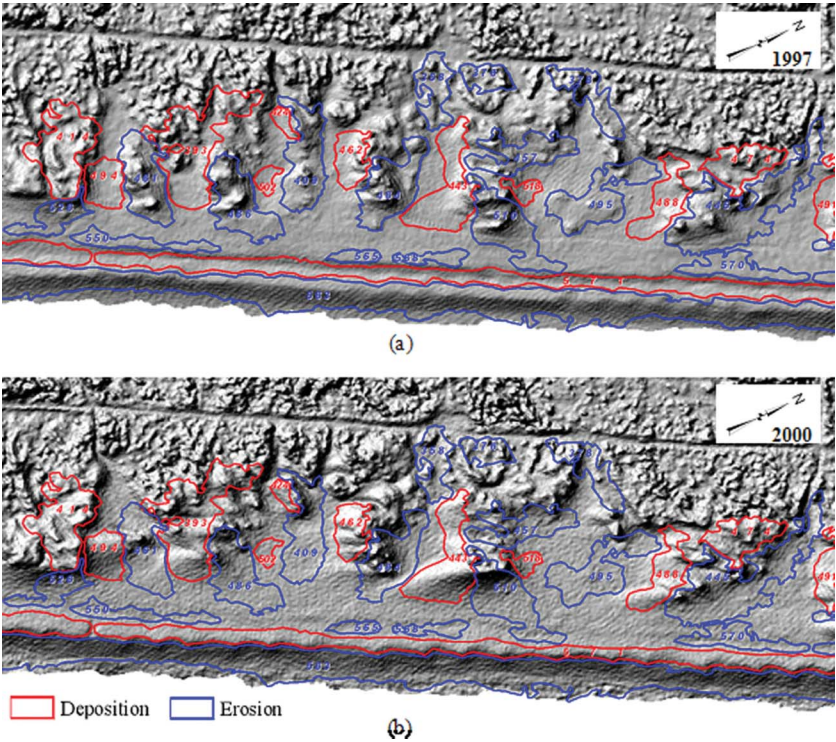


Figure 9. Erosion and deposition objects overlain on the hill-shaded relief images. (a) Relief image derived from 1997 LiDAR data; (b) relief image derived from 2000 LiDAR data.

volume is estimated to be 28,223 m³. The net erosion volume is 38,371 m³. The normalized annual net erosion volume rate is 6.91 m³ per meter of the shoreline stretch for Assateague Island. The localized information about morphological and volumetric changes should be useful for measuring, understanding, and predicting coastal morphological changes and designing future erosion control projects, such as beach nourishments and dune management.

8. Conclusion

Erosion hazards and landward retreat of shorelines have imposed severe damages and threats to coastal properties, public safety, and the coastal tourism economies. Frequent and timely measurements of coastal morphology are required for the accurate assessment and prediction of hazard damages and the design of intelligent management policies to protect coastal communities and to promote the wise use of coastal resources. Airborne LiDAR technology has provided an efficient and highly accurate means to survey coastal morphology over large areas. The increasing availability of airborne LiDAR data calls for efforts to develop a new conceptual framework and efficient computational methods for extracting morphological information and knowledge from massive raw data sets.

In this research, we have developed a general analytical framework for object-based morphological analysis. A numerical algorithm is developed to construct explicit and meaningful morphological objects from raw spatial data, which are ontologically and epistemologically important for describing and interpreting the dynamics of coastal

morphology. This method essentially reduces a large volume of cell-by-cell elevation difference values into a higher level of concise representation of erosion and deposition objects. Object-based representation is more consistent and compatible with the perception and cognition of human analysts and of geomorphologists. The use of erosion and deposition objects as the basic spatial unit reduces the influence of data noise and enhances the reliability of extracted morphological information. It also makes it easy to eliminate spurious changes. Compared with grid cells in the field-based representation, objects are much better information carriers. In addition to the elevation information, various planimetric and shape attributes, surface and volumetric attributes can be derived for erosion and deposition objects. These attributes capture the fundamental aspects of the changing coastal morphology at a fine scale.

When the generalization is applied to the original field-based data in the process of object extraction and formation, the information about the subtle within-object variations and heterogeneity is lost. As the process of object extraction is carried out, more attributes are encapsulated in the objects and the level of semantics and knowledge will be increased and accumulated. It should be emphasized that the loss of precision is overwhelmed by the increased utility that the derived objects can provide. The analysis of the erosion and deposition object attributes allows insight into the sedimentary processes that shape and modify coastal morphology at various time scales. As demonstrated with our example, our object-based method and software package provide a powerful tool for the geosciences and coastal research community to process high-resolution sequential airborne LiDAR data sets for coastal morphological and volumetric change analysis. When this tool is used with a shoreline detection method, such as that described in Liu *et al.* (2007), overall magnitudes of coastal changes and evolutions will be much more easily quantified.

Acknowledgments

This research is funded by the NOAA Sea Grant Program #NA16RG1078 and Texas Advanced Research Program (TARP). Comments and suggestions from Professor May Yuan and three anonymous reviewers have been very helpful in improving the quality of this article.

References

- Andrews, B.D., Gares, P.A., and Colby, J.D., 2002. Techniques for GIS modeling of coastal dunes. *Geomorphology*, 48, 289–308.
- Arctur, D. and Zeiler, M., 2004. *Designing geodatabases: case studies in GIS data modeling*. Redland, CA: ESRI Press.
- Baatz, M., *et al.*, 2001. *eCognition object oriented image analysis, user guide*. München, Germany: Definiens Imaging.
- Bauer, B.O. and Davidson-Arnott, R.G.D., 2003. A general framework for modeling sediment supply to coastal dunes including wind angle, beach geometry, and fetch effects. *Geomorphology*, 49, 89–108.
- Bian, L., 2000. Object-oriented representation for modelling mobile objects in an aquatic environment. *International Journal of Geographical Information Science*, 14 (7), 603–623.
- Bian, L., 2007. Object-oriented representation of environmental phenomena: is everything best represented as an object? *Annals of the Association of American Geographers*, 97 (2), 267–281.
- Blaschke, T. and Strobl, J., 2001. What's wrong with pixels? Some recent developments interfacing remote sensing and GIS. *Zeitschrift für Geoinformationssysteme*, 6 (2001), 12–17.
- Brock, J.C., Krabill, W.B., and Sallenger, A.H., 2004. Barrier island morphodynamic classification based on lidar metrics for north Assateague Island, Maryland. *Journal of Coastal Research*, 20 (2), 498–509.
- Burrough, P.A., 1981. Fractal dimensions of landscapes and other environmental data. *Nature*, 294, 240–242.

- Câmara, G., Freitas, U., and Casanova, M.A., 1995. Fields and objects algebras for GIS operations. *Proceedings of III Brazilian Symposium on GIS*. University Park, PA, Citeseer. 407–424.
- Castilla, G. and Hay, G.J., 2008. Image objects and geographic objects. In: T. Blaschke, S. Lang, and G.J. Hay, eds. *Object-based image analysis*. Berlin: Springer, 91–110.
- Chaudhuri, D. and Samal, A., 2007. A simple method for fitting of bounding rectangle to closed regions. *Pattern Recognition*, 40 (7), 1981–1989.
- Couclelis, H., 1992. People manipulate objects (but cultivate fields): beyond the raster–vector debate in GIS. *Lecture Notes in Computer Science*, 639, 65–65.
- Cova, T.J. and Goodchild, M.F., 2002. Extending geographical representation to include fields of spatial objects. *International Journal of Geographical Information Science*, 16 (6), 509–532.
- Davis, J.C., 2002. *Statistics and data analysis in geology*. 3rd ed. New York: John Wiley & Sons, Inc.
- Dolan, R., Fenster, M., and Holme, S., 1991. Temporal analysis of shoreline recession and accretion. *Journal of Coastal Research*, 7 (3), 723–744.
- Egenhofer, M.J. and Frank, A., 1987. Object-oriented databases: database requirements for GIS. *International Geographic Information Systems (IGIS) Symposium: The Research Agenda*. Arlington, VA, 189–211.
- Egenhofer, M.J. and Frank, A.U., 1992. Object-oriented modeling for GIS. *URISA Journal*, 4 (2), 3–19.
- Finkl, C.W., Benedet, L., and Andrews, J.L., 2005. Interpretation of seabed geomorphology based on spatial analysis of high-density airborne laser bathymetry. *Journal of Coastal Research*, 21 (3), 501–514.
- Fitzgibbon, A., Pilu, M., and Fisher, R.B., 1999. Direct least square fitting of ellipses. *IEEE Transactions on Pattern Analysis and Machine Intelligence*, 21 (5), 476–480.
- Flusser, J. and Suk, T., 1993. Pattern recognition by affine moment invariants. *Pattern Recognition*, 26 (1), 167–174.
- Forman, R.T.T., 1995. *Land Mosaics*. Cambridge: Cambridge University Press.
- Foroutan-pour, K., Dutilleul, P., and Smith, D.L., 1999. Advances in the implementation of the box-counting method of fractal dimension estimation. *Applied Mathematics and Computation*, 105 (2–3), 195–210.
- Gahegan, M., 1996. Specifying the transformations within and between geographic data models. *Transactions in GIS*, 1, 137–152.
- Galton, A., 2001. Space, time, and the representation of geographical reality. *Topoi*, 20 (2), 173–187.
- Galton, A., 2004. Fields and objects in space, time, and space-time. *Spatial Cognition & Computation*, 4 (1), 39–68.
- Gares, P.A., Wang, Y., and White, S.A., 2006. Using LiDAR to monitor a beach nourishment project at Wrightsville Beach, North Carolina, USA. *Journal of Coastal Research*, 22 (5), 1206–1219.
- Goodchild, M.F., 1992. Geographical data modeling. *Computers & Geosciences*, 18 (4), 401–408.
- Goodchild, M.F., Yuan, M., and Cova, T.J., 2007. Towards a general theory of geographic representation in GIS. *International Journal of Geographical Information Science*, 21 (3), 239–260.
- Gutierrez, R., et al., 2001. Precise airborne lidar surveying for coastal research and geo-hazards applications. *International Archives of Photogrammetry and Remote Sensing*, XXXIV-3/W4, 185–194.
- Hesp, P.A., et al., 2005. Flow dynamics over a foredune at Prince Edward Island, Canada. *Geomorphology*, 65, 71–84.
- Leung, Y., Leung, K.S., and He, J.Z., 1999. A generic concept-based object-oriented geographical information system. *International Journal of Geographical Information Science*, 13 (5), 475–498.
- Liu, H. and Jezek, K.C., 2004. Automated extraction of coastline from satellite imagery by integrating Canny edge detection and locally adaptive thresholding methods. *International Journal of Remote Sensing*, 25 (5), 937–958.
- Liu, H., Sherman, D., and Gu, S., 2007. Automated extraction of shorelines from airborne light detection and ranging data and accuracy assessment based on Monte Carlo simulation. *Journal of Coastal Research*, 23, 1359–1369.
- Mandelbrot, B.B., 1983. *The fractal geometry of nature*. New York: W.H. Freeman and Company.
- McGarigal, K., et al., 2002. FRAGSTATS: spatial pattern analysis program for categorical maps. Computer software program produced by the authors at the University of Massachusetts, Amherst. Available from: <http://www.umass.edu/landeco/research/fragstats/fragstats.html> [Accessed 20 July 2009].
- McGarigal, K. and Marks, B.J., 1995. *FRAGSTATS: spatial pattern analysis program for quantifying landscape structure*. Gen. Tech. Rep. PNW-GTR-351, 122. U.S. Department of Agriculture, Forest Service, Pacific Northwest Research Station.

- Mulchrone, K.F. and Choudhury, K.R., 2004. Fitting an ellipse to an arbitrary shape: implications for strain analysis. *Journal of Structural Geology*, 26 (1), 143–153.
- Parker, B.B., 2003. The difficulties in measuring a consistently defined shoreline: the problem of vertical referencing. *Journal of Coastal Research*, 38, 44–56.
- Peuquet, D.J., 1988. Representations of geographic space: toward a conceptual synthesis. *Annals of the Association of American Geographers*, 78 (3), 375–394.
- Peuquet, D.J., 1994. Its about time – a conceptual-framework for the representation of temporal dynamics in geographic information-systems. *Annals of the Association of American Geographers*, 84 (3), 441–461.
- Pratt, W.K., 1991. *Digital image processing*. 2nd ed. New York: John Wiley & Sons, Inc.
- Raper, J. and Livingstone, D., 1995. Development of a geomorphological spatial model using object-oriented design. *International Journal of Geographical Information Systems*, 9 (4), 359–383.
- Rosin, P.L., 1993. Ellipse fitting by accumulating five-point fits. *Pattern Recognition Letters*, 14 (8), 661–669.
- Rosin, P.L., 2003. Measuring shape: ellipticity, rectangularity, and triangularity. *Machine Vision and Applications*, 14 (3), 172–184.
- Sallenger, A.H., et al., 2003. Evaluation of airborne topographic lidar for quantifying beach changes. *Journal of Coastal Research*, 19 (1), 125–133.
- Sherman, D.J. and Bauer, B.O., 1993. Dynamics of beach-dune systems. *Progress in Physical Geography*, 17, 413–447.
- Shrestha, R.L., et al., 2005. Airborne laser swath mapping: quantifying changes in sandy beaches over time scales of weeks to years. *ISPRS Journal of Photogrammetry and Remote Sensing*, 59 (4), 222–232.
- Smith, B. and Mark, D.M., 2003. Do mountains exist? Towards an ontology of landforms. *Environment and Planning B-Planning & Design*, 30 (3), 411–427.
- Sonka, M., Hlavac, V., and Boyle, R., 1999. *Image processing, analysis, and machine vision*. 2nd ed. Pacific Grove: Brooks/Cole Publishing Company.
- Suesse, H. and Voss, K., 2001. *A new efficient algorithm for fitting of rectangles and squares*. Thessaloniki City: Institute of Electrical and Electronics Engineers Computer Society, 2, 809–812.
- Tang, A.Y., Adams, T.M., and Usery, E.L., 1996. A spatial data model design for feature-based geographical information systems. *International Journal of Geographical Information Systems*, 10 (5), 643–659.
- Teague, M.R., 1980. Image-analysis via the general theory of moments. *Journal of the Optical Society of America*, 70 (8), 920–930.
- Turner, M.G. and Gardner, R.H., eds., 1991. *Quantitative methods in landscape ecology*. New York: Springer-Verlag.
- Turner, M.G., Gardner, R.H., and O'Neill, R.V., 2001. *Landscape ecology in theory and practice*. New York: Springer-Verlag.
- Usery, E., 1993. Category theory and the structure of features in geographic information systems. *Cartography and Geographic Information Science*, 20 (1), 5–12.
- Usery, E.L., 1996. A conceptual framework and fuzzy set implementation for geographic features. In: P.A. Burrough and A.U. Frank, eds. *Geographic objects with indeterminate boundaries*. London: Taylor & Francis, 71–86.
- White, S.A. and Wang, Y., 2003. Utilizing DEMs derived from LIDAR data to analyze morphologic change in the North Carolina coastline. *Remote Sensing of Environment*, 85 (1), 39–47.
- Worboys, M.F., 1994. Object-oriented approaches to geo-referenced information. *International Journal of Geographical Information Systems*, 8 (4), 385–399.
- Wright, L.D. and Short, A.D., 1984. Morphodynamic variability of surf zones and beaches: a synthesis. *Marine Geology*, 56 (1–4), 93–118.
- Wynn, T.J. and Stewart, S.A., 2005. Comparative testing of ellipse-fitting algorithms: implications for analysis of strain and curvature. *Journal of Structural Geology*, 27 (11), 1973–1985.
- Zhang, K., et al., 2005. Quantification of beach changes caused by hurricane Floyd along Florida's Atlantic Coast using airborne laser surveys. *Journal of Coastal Research*, 21 (1), 123–134.